water

MDPI

Article

Synchronized Structure and Teleconnection Patterns of Meteorological Drought Events over the Yangtze River Basin, China

Lei Liu [1,2,3], Chao Gao [2,3], Zhanliang Zhu [1,2,3], Xiongpeng Tang [2,3], Dongjie Zhang [1,*] and Silong Zhang [2,3]

[1] Hubei Key Laboratory of Intelligent Yangtze and Hydroelectric Science, China Yangtze Power Co., Ltd., Yichang 443000, China
[2] College of Water Sciences, Beijing Normal University, Beijing 100875, China
[3] Center for Water Research, Advanced Institute of Natural Sciences, Beijing Normal University, Zhuhai 519087, China
* Correspondence: zhang_dongjie1@ctg.com.cn

Abstract: Investigating the synchronized structure and teleconnection patterns of meteorological drought events (MDEs) contributes to elucidating drought's evolution. In this study, the CN05.1 gridded meteorological dataset from 1961 to 2021 was utilized to calculate the 3-month standardized precipitation evapotranspiration index (SPEI-3) for each grid in the Yangtze River Basin (YRB). Based on these SPEI-3 series, the grid-based MDEs were then extracted. Subsequently, event synchronization and complex networks were employed to construct the MDE synchronized network over the YRB. This network was used to identify the MDEs' topological structure, synchronized subregions, and representative grids. Finally, the MDE characteristics and MDE teleconnection patterns of individual subregions were investigated. The results of the MDE topological structure show that the northeastern portion of the YRB tends to experience widespread MDEs, while specific areas in the upper reaches are prone to localized MDEs. Synchronous MDEs mainly propagate along the central pathway and the eastern pathway, which display relatively low MDE spatial coherence. The YRB is partitioned into eight MDE synchronized subregions, each exhibiting distinct characteristics in terms of the frequency, duration, total severity, and peak of MDEs, as well as MDE temporal frequency distributions. Among all teleconnection factors, El Niño–Southern Oscillation (ENSO) exerts a strong influence on MDEs in all subregions, the Pacific Decadal Oscillation (PDO) shows a significant association with MDEs in all subregions except for Subregion 3 in the southeast, the North Atlantic Oscillation (NAO) displays a significant influence on MDEs in the southern subregions of the YRB, and the Arctic Oscillation (AO) has a more pronounced influence on MDEs in the northern subregions. This study provides valuable insights on drought's evolution within the YRB and offers guidance to policymakers for advanced preventive measures.

Keywords: meteorological drought; event synchronization; complex network; teleconnection; Yangtze River Basin

check for updates

Citation: Liu, L.; Gao, C.; Zhu, Z.; Tang, X.; Zhang, D.; Zhang, S. Synchronized Structure and Teleconnection Patterns of Meteorological Drought Events over the Yangtze River Basin, China. *Water* **2023**, *15*, 3707. https://doi.org/10.3390/w15213707

Academic Editor: Athanasios Loukas

Received: 25 September 2023
Revised: 19 October 2023
Accepted: 20 October 2023
Published: 24 October 2023

Copyright: © 2023 by the authors. Licensee MDPI, Basel, Switzerland. This article is an open access article distributed under the terms and conditions of the Creative Commons Attribution (CC BY) license (https://creativecommons.org/licenses/by/4.0/).

1. Introduction

Drought, as one of the most pervasive, frequent, and devastating types of natural disaster worldwide, has experienced exacerbation in recent years due to global climate change and intensified anthropogenic disturbances [1–3]. The changing environment has resulted in spatiotemporal variations in precipitation, evapotranspiration, runoff, and associated water-cycle processes, and the occurrence and evolution of droughts have also been changed [4–7]. Globally, there is an increasing trend in the length of dry spells and the frequency of droughts, particularly large-scale synchronous droughts, leading to significant impacts on regional water resource management, terrestrial ecosystems, and socioeconomic sustainability [8–12]. For instance, during the summer of 2022, multiple

regions within the Yangtze River Basin (YRB) simultaneously experienced the most severe meteorological drought since 1961. This event caused substantial economic and social consequences, including water shortages, electricity supply disruptions, livestock water-source interruptions, and crop yield reductions [13]. Given the escalating impacts of drought, understanding the evolving dynamics of drought becomes vital to mitigate drought disasters and protect ecosystems [14].

Drought evolution represents the dynamic development process, involving both the spatial and temporal dimensions [15]. Compared to the evolution processes of other extreme hydroclimatic events, drought's evolution exhibits heightened spatiotemporal complexity, often persisting for several months to years and spanning hundreds to thousands of kilometers [16–18]. Moreover, it is widely acknowledged that drought typically originates from prolonged deficits in precipitation, known as meteorological drought, and this may subsequently evolve into potential soil moisture deficits (agricultural drought), reductions in surface runoff or groundwater (hydrological drought), and inadequate water supply for socioeconomic demands (socioeconomic drought) with the exacerbation of meteorological drought through large-scale atmospheric circulation processes and the hydrological cycle [19–21]. Among these various types of drought, meteorological drought serves as the earliest occurrence type, and the other types are usually the serious consequences of its impacts [22–24]. Hence, a thorough analysis of the spatiotemporal evolution of meteorological drought not only aids in predicting the occurrence of other drought types but also enhances drought prevention and mitigation efforts to minimize socioeconomic losses.

Several meteorological drought indices based on water deficit have been employed to identify meteorological drought events (MDEs), including the standardized precipitation index (SPI), standardized precipitation evapotranspiration index (SPEI) [25], Palmer drought severity index (PDSI) [26], and meteorological drought composite index (MCI) [27]. These objective and quantitative indices are effective tools for assessing the status and characteristics of meteorological drought, enabling the quantification of temporal characteristics such as the frequency, intensity, duration, and severity of MDEs [28–30]. In addition to temporal variability, many existing studies have characterized the spatial behaviors of MDEs using severity–area–duration (SAD) and severity–area–frequency (SAF) curves, offering valuable insights into the spatial evolution of MDEs in terms of centroid, displacement, and direction [31–34]. For instance, Palazzolo et al. [34] introduced a probabilistic framework to describe the SPEI-based SAF curves, aiming to assess the drought severity as a function of the SPEI at the regional scale and link it to the spatial extent of the affected area. Nonetheless, the spatiotemporal topological structure of MDEs over large-scale areas (i.e., the association relationships of synchronous MDE occurrences) and the involved spatial extents of synchronous MDEs still remain unclear. Investigating the MDEs' synchronized structure is key to quantifying the looming risks of large-scale droughts and their resulting impacts [35,36].

To reveal the MDEs' synchronized structure over large-scale areas, it is crucial to analyze the MDEs' synchronization between different locations, which signifies the temporal co-occurrences of MDEs at these locations. Large-scale occurrences of synchronous MDEs often display certain spatial connections; thus, understanding the MDEs' synchronization within large-scale areas is beneficial for identifying the MDEs' synchronized structure. However, quantifying the MDEs' synchronization is challenging and requires specific statistical and dynamical methodologies [37]. In recent years, complex network (CN) theory has provided new perspectives [18]. The CN is a collection of nodes linked by edges and is capable of depicting intricate relationships within complex dynamical systems [37]. It has progressively been utilized to indicate the MDE synchronization in various drought systems [35,36,38]. For example, Mondal et al. [35] quantified the spatial synchronization structure of global MDE occurrences and revealed multiple spatial scales associated with drought centers. Konapala et al. [36] further constructed regional drought networks and explored the spatiotemporal structure and driving mechanisms of MDEs' evolution in North America. Jha et al. [38] utilized a CN to construct an undirected network to assess

the spatiotemporal characteristics of MDEs driven by Indian precipitation in past and future climatic scenarios. In summary, CNs offer significant potential for quantifying the MDEs' synchronized structure. However, there is currently limited research in the context of China [39].

The YRB, as the largest river basin in China, plays multiple roles in China's social development, including economic centers, cultural inheritance, ecological importance, and policy attention [40]. Given the increasing frequency and intensity of MDEs across the YRB, along with their potential exacerbation in the future [41], understanding the MDEs' synchronized structure over the YRB becomes critically important. Additionally, MDEs occurring in different parts of the YRB are associated with the influence of a range of teleconnection patterns [42]. Therefore, it is imperative to explore the influence effects of diverse teleconnection factors on MDEs occurring in distinct regions. This study focuses on identifying the MDEs' synchronized structure within the YRB by employing the CN theory and further investigating the influence effects of teleconnection factors on MDEs within various regions. The main objectives of this study are (1) to investigate the MDEs' synchronized structure over the YRB, (2) to identify the MDEs' synchronized subregions over the YRB, and (3) to explore the MDE teleconnection patterns of individual subregions. The proposed methodology and findings in this study are expected to contribute to a better understanding of the spatial aspects of MDEs' occurrences and evolution in the YRB.

2. Study Area and Data

As the third-largest basin globally and the largest basin in China, the YRB, depicted in Figure 1, was selected as the study area in this study. Its expansive drainage area spans approximately 1.8 million km^2, constituting around one-fifth of China's mainland territory [43]. This basin is situated within a humid and semi-humid region with a remarkable monsoon climate. This implies that its response to climate change is intricate and volatile, as reflected in drought events with short-term fluctuations [44]. Consequently, it is susceptible to recurring seasonal drought events [45].

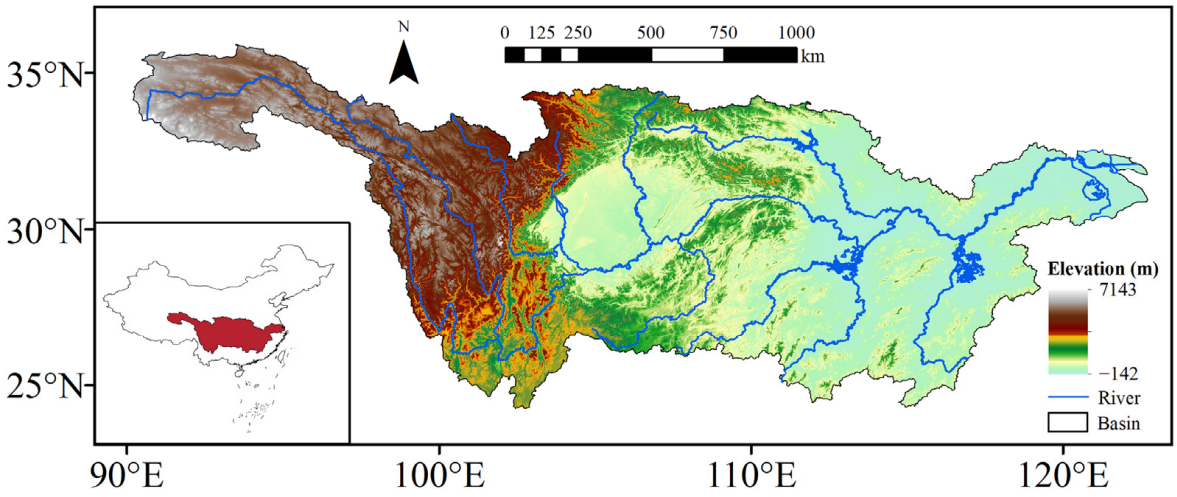


Figure 1. Location and elevation of the Yangtze River Basin (YRB).

The standardized precipitation evapotranspiration index (SPEI) was adopted in this study to evaluate dry or wet conditions and capture MDEs in the YRB. The SPEI, in comparison to the conventional standardized precipitation index (SPI), incorporates the influence of evapotranspiration on drought severity. This attribute makes the SPEI particularly adept at reflecting the broader impacts of drought on hydrological systems and ecosystems [25]. Furthermore, the SPEI offers the advantage of featuring multiple timescales, and the 3-month SPEI (SPEI-3), delineating seasonal-scale variations in dry and wet conditions, is particularly suitable for characterizing the spatiotemporal evolution of MDEs [43]. To

calculate the SPEI-3 index, the CN05.1 gridded meteorological dataset was employed in this study, including monthly precipitation and monthly mean temperature data from 1961 to 2021. The CN05.1 dataset, with a spatial resolution of 0.25° × 0.25°, provides a precise representation of meteorological elements' variations. It was released by the National Climate Center and constructed using advanced techniques, including thin plate spline interpolation and angular distance weighting methods, based on observation data from over 2400 national stations [46]. As a result, a total of 2666 grids were extracted within the YRB.

To investigate the MDE teleconnection patterns of the MDE synchronized subregions, four large-scale climate indices spanning the period from 1961 to 2021 were selected. These indices were El Niño–Southern Oscillation (ENSO), the Pacific Decadal Oscillation (PDO), the North Atlantic Oscillation (NAO), and the Arctic Oscillation (AO). Further details regarding the data are provided in Table 1.

Table 1. Data description for teleconnection factors.

Teleconnection Factors	Time Frame	Data Source	Access Date
ENSO	1961–2021	http://www.esrl.noaa.gov/psd/data/correlation/nina34.data	22 October 2023
PDO	1961–2021	http://www.ncdc.noaa.gov/teleconnections/pdo/	22 October 2023
NAO	1961–2021	https://www.ncdc.noaa.gov/teleconnections/nao/	22 October 2023
AO	1961–2021	https://www.ncdc.noaa.gov/teleconnections/ao/	22 October 2023

3. Methodology

The research flowchart shown in Figure 2 encompasses the following sequential steps: First, the grid-based MDEs are extracted based on the SPEI-3 series to obtain corresponding sequences of MDE occurrences. Subsequently, the MDE synchronized network over the YRB is constructed based on the MDE synchronized matrix, as depicted by the schematic diagram of network construction. Based on the constructed network, the MDE synchronized structure, MDE synchronized subregions, and MDE teleconnection patterns of individual subregions are finally identified.

3.1. Extraction of Grid-Based MDEs and Relevant MDE Characteristics over the YRB by Run Theory

SPEI values falling below −1 indicate the presence of moderate-to-more-severe drought conditions. Additionally, it is recognized that short-term droughts (e.g., droughts lasting for 1 or 2 months) may signify less severe drought conditions [29,36]. Consequently, in this study, MDEs were extracted based on SPEI-3 values falling below -1 with a minimum duration of seasonal scale (i.e., 3 months), as shown by the orange-shaded regions in Figure 3. For each grid in the YRB, the MDE occurrence time is defined as the first occurrence month of SPEI-3 values less than −1, as illustrated by the red line in Figure 3.

To estimate the temporal characteristics of MDE occurrences across the YRB, four relevant MDE characteristics (frequency, duration, total severity, and peak) for individual grids were calculated based on run theory in this study. The MDE frequency corresponds to the number of MDE occurrences within a given period. As shown in Figure 3, grids *i* and *j* exhibit MDE frequencies of 4 and 6 times, respectively. The MDE duration refers to the number of months within a single MDE, while the MDE total severity represents the cumulative deficit below the critical value −1 throughout one MDE. Additionally, the MDE peak signifies the maximum gap between the SPEI value and the critical value −1 during a single MDE [47,48]. The identified duration, total severity, and peak of the first MDE at grid *i* are represented in the upper subplot of Figure 3.

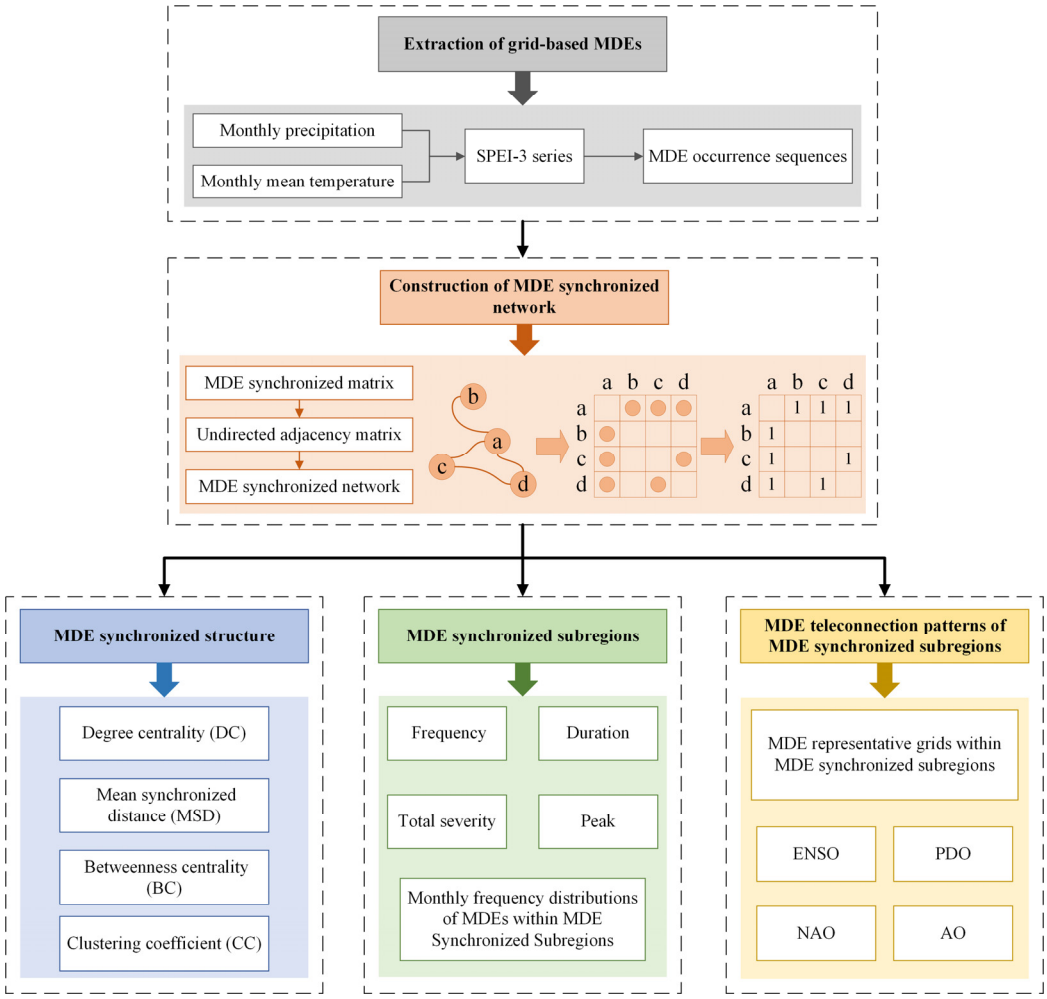


Figure 2. Flowchart of this study.

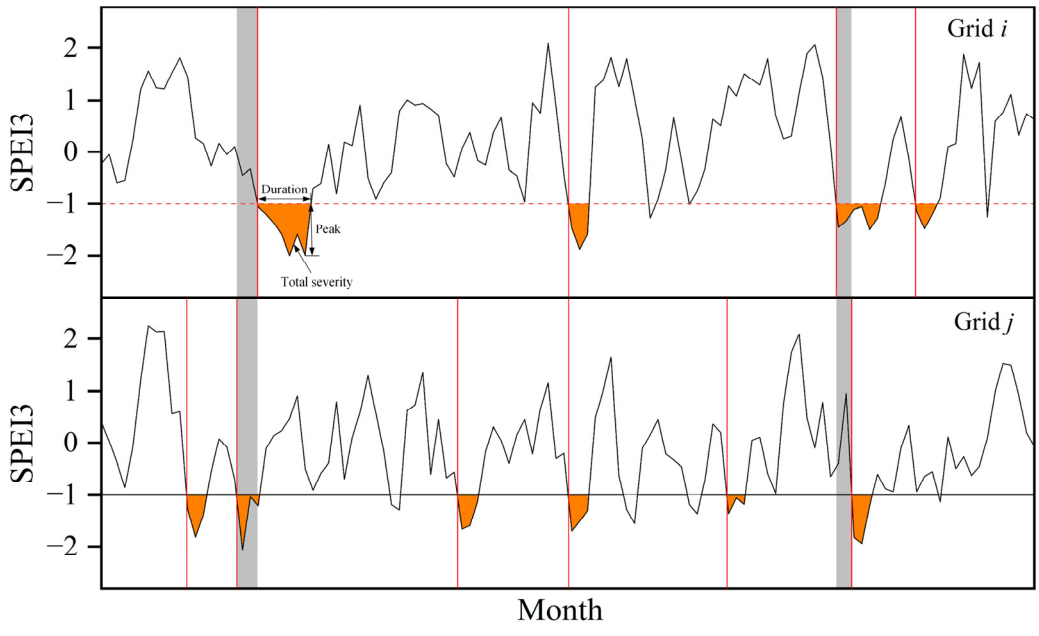


Figure 3. Hypothetical demonstration for extracting meteorological drought events (MDEs) based on the series of 3-month standardized precipitation evapotranspiration index (SPEI-3) of grids *i* and *j*.

The upper and lower subplots represent the SPEI-3 series of grids i and j, respectively. The orange-shaded regions denote the extracted MDEs with a duration of no less than 3 months. The numbers of MDEs at grid i and grid j are 4 and 6, respectively. The red lines indicate the occurrence time of the MDEs. The gray-shaded regions show three groups of synchronously occurring MDEs at grids i and j, where the first group presents the MDE at grid i occurring later than that at grid j, the second group shows the MDEs at both grids occurring simultaneously, and the last group exhibits the MDE at grid i occurring earlier than that at grid j. The identified duration, total severity, and peak of the first MDE of grid i are also represented in the upper subplot.

3.2. Calculation of the MDE Synchronized Matrix over the YRB by Event Synchronization (ES)

ES measures time-lagged correlations between various event sequences, offering an effective way to capture their corresponding synchronization [49]. In this study, the ES method was employed to quantify the MDEs' synchronized strength between grid pairs. In contrast to other time-lagged methods such as Pearson's correlation, ES is suitable for cases involving dynamic time delays between event sequences. Furthermore, it does not assume any specific probability distribution for the event sequences to follow [50]. This property allows for more accurate analysis of nonlinear relationships and facilitates a more effective capture of the underlying dynamics of MDE occurrences. Therefore, ES is particularly suitable for the analysis of the MDE occurrence sequences, where the MDEs may occur at irregular intervals due to varying climatic conditions and other factors.

ES was utilized to measure the MDEs' synchronized strength between grids i and j by calculating the number of time-coincident MDEs with dynamic delays. Let $E_i = \left\{t_l^i\right\}, \left(t_l^i < t_{l+1}^i, l = 1, 2, \cdots, n_i\right)$ and $E_j = \left\{t_m^j\right\}, \left(t_m^j < t_{m+1}^j, m = 1, 2, \cdots, n_j\right)$ represent the MDE occurrence sequences at grids i and j, respectively, where t_l^i and t_m^j denote the lth occurrence time of MDEs in E_i and the mth occurrence time of MDEs in E_j, respectively. Furthermore, n_i and n_j represent the total number of extracted MDEs for grids i and j, respectively. The dynamic delay τ_{lm}^{ij} of MDEs occurring at t_l^i and t_m^j is defined as follows:

$$\tau_{lm}^{ij} = \frac{\min\left\{t_{l+1}^i - t_l^i, t_l^i - t_{l-1}^i, t_{m+1}^j - t_m^j, t_m^j - t_{m-1}^j\right\}}{2} \tag{1}$$

In order to exclude unreasonably long dynamic delays, a maximum time delay of 3 months (i.e.,$\tau_{\max}$ = 3) was set. When $\left|t_l^i - t_m^j\right| \in \left[0, \tau_{lm}^{ij}\right) \cap [0, \tau_{\max}]$, it is considered that the lth MDE at grid i occurs synchronously with the mth MDE at grid j; $c(i|j)$ is defined as the number of MDEs at grid i that always occur after those at grid j, and $c(j|i)$ is the contrary; $c(i|j)$ is denoted as follows:

$$c(i|j) = \sum_{l=1}^{n_i} \sum_{m=1}^{n_j} J_{ij} \tag{2}$$

where

$$J_{ij} = \begin{cases} 1 & if\ 0 < t_l^i - t_m^j < \tau_{lm}^{ij} \text{ and } 0 < t_l^i - t_m^j \le \tau_{\max} \\ 0.5 & if\ t_l^i = t_m^j \\ 0 & if\ otherwise \end{cases} \tag{3}$$

Accordingly, $c(j|i)$ can also be defined. The MDEs' synchronized strength Q_{ij} between grids i and j is defined as follows:

$$Q_{ij} = \frac{c(i|j) + c(j|i)}{\sqrt{n_i n_j}} \tag{4}$$

where $Q_{ij} \in [0,1]$; $Q_{ij} = 1$ indicates complete MDE synchronization between grids i and j, while $Q_{ij} = 0$ stands for the absence of MDE synchronization. Repeat the procedure described above for all pairwise grids within the YRB, and the MDE synchronized matrix Q can be obtained. This matrix is square and symmetric, representing the MDEs' synchronized patterns between different grid locations.

3.3. Construction of the MDE Synchronized Network over the YRB by a Complex Network (CN)

Based on the Q matrix, the MDE synchronized network over the YRB was constructed to encode the MDEs' synchronized relationships between various grids. In this network, each grid was considered as a node, and edges were established to encode significant MDE synchronization between various grids. To ensure that the MDEs' synchronized strength values were extracted with high statistical significance, a threshold approach was adopted to establish edges. It was assumed that the linked edges are only established when the MDEs' synchronized strength between node pairs exceeds a given threshold. Specifically, the 95th percentile of all non-zero values in Q was selected as the threshold θ^Q [51]. In other words, only the highest5% MDE synchronized strength values between all node pairs remained and were utilized to build the undirected adjacency matrix A^Q, which is expressed as follows:

$$A_{ij}^{Q} = \begin{cases} 1 & if\ Q_{ij} > \theta^{Q} \\ 0 & if\ otherwise \end{cases} \tag{5}$$

where $A_{ij}^{Q} = 1$ means that the linked edge between nodes i and j exists. In the current study, the value of θ^Q is 0.865. Furthermore, to assess the statistical significance of these linked edges, a test based on independent and uniformly random distribution of events from the work of Boers et al. [52] was employed. The test yielded probability values of 0.01 for θ^Q. Thus, all linked edges corresponded to significant values of ES. Based on the A^Q matrix, the MDE synchronized network over the YRB was constructed, which contained the synchronized MDE information between grid pairs within the YRB.

3.4. Quantification of MDEs' Synchronized Structure over the YRB by Network-Based Metrics

In this study, four network metrics were computed based on the MDE synchronized network over the YRB: degree centrality (DC), mean synchronized distance (MSD), betweenness centrality (BC), and clustering coefficient (CC). These four metrics can be found in previous climate CN literature [18,52–54]. They were used to quantify the MDEs' synchronized structure across the YRB. The detailed description of these metrics is below:

(1) Degree k_i measures the number of edges that node i has in the network; these connected nodes make up the adjacent nodes of node i. Degree centrality DC_i is the normalized result of k_i, which is formulated as follows:

$$DC_i = \frac{\sum_{j=1}^{N-1} A_{ij}^{Q}}{N-1} \tag{6}$$

where N is the total number of nodes in the network. In this study, a region with higher DC values signifies more significant connections to other nodes within the whole network, suggesting a greater area of synchronization in terms of MDE occurrences.

(2) MSD represents the average geographic distance between a node and its adjacent nodes in the network. MSD_i can be mathematically expressed as follows:

$$MSD_i = \frac{\sum_{j=1}^{N-1} A_{ij}^{Q} d_{ij}}{\sum_{j=1}^{N-1} A_{ij}^{Q}} \tag{7}$$

where d_{ij} represents the geographic distance between node i and its adjacent node j. In the network, the MSD of a node provides insights into its spatial extent of MDE synchronization.

(3) BC is a metric that identifies nodes that act as intermediaries or bridges in the network. BC_i is defined as the proportion of the shortest path number between node pairs passing through node i to the total number of the shortest paths of these node pairs in the network, which is shown as follows:

$$BC_i = \frac{\sum\limits_{s \neq i \neq t} \sigma_{st}(i)}{\sum\limits_{s \neq i \neq t} \sigma_{st}} \tag{8}$$

where $\sigma_{st}(i)$ represents the number of the shortest paths between node s and node t passing through node i, and σ_{st} represents the number of the shortest paths between node s and node t, where nodes s and t belong to any pair of nodes in the network. In the context of the MDE synchronized network over the YRB, the BC quantifies the extent to which a grid location lies on the shortest paths connecting all of the other grid locations. Regions with higher BC values are more likely to serve as pathways for the propagation of synchronous MDEs within the network.

(4) The CC of a node measures the proportion of its neighbors that are also connected to one another, which is defined as follows:

$$CC_i = \frac{2\beta}{k_i(k_i - 1)} \tag{9}$$

where k_i is the degree of node i, while β and $k_i(k_i - 1)/2$ represent the actual number of edges and the maximum possible number of edges among the adjacent nodes of node i, respectively. In the MDE synchronized network, a high CC value for a node suggests that the nodes in its neighborhood are closely interconnected, displaying spatial coherence in the MDE occurrences. However, events in such regions are less likely to synchronize with geographically distant neighbors.

It should be noticed that for the constructed MDE synchronized network over the YRB, the geographic boundaries of the YRB were artificially embedded, which cut off the edges connecting specific nodes within this basin to the outside nodes. This configuration may affect the accuracy of certain network metrics [55]. To correct the potential boundary effect, the spatially embedded random networks method was introduced in this study [56]. It was assumed that the edges that were disconnected due to the boundary effect could be reconnected by randomly generating surrogate networks that followed approximately the same link probability distributions depending on the spatial link lengths as those of the original network. In this study, 100 random surrogate networks were generated to ensure stable estimations of the boundary effect. For each surrogate network, the same network metrics were calculated, just as in the original network. The average value of each metric calculated in these surrogate networks was then used to estimate the boundary effect, which was defined as the boundary-affected metric [56,57]. The corrected network metric M_c was obtained by dividing the uncorrected (original) metric M_u by the boundary-affected metric from the 100 surrogate networks M_b, as shown below:

$$M_c = \frac{M_u}{M_b} \tag{10}$$

According to the definitions of the metrics mentioned above, it is evident that the DC, CC, and BC are susceptible to the boundary effect, while the MSD is almost unaffected by the boundary effect [53]. By correcting the DC, CC, and BC metrics, more accurate and meaningful results of these MDE topological properties could be obtained in this study. Furthermore, the corrected network metrics were ranked based on the empirical

distribution of the samples and normalized to [0, 1]. By ranking and normalizing these metrics, this study aims to obtain reliable and comparable results.

3.5. Partitioning of MDE Synchronized Subregions within the YRB by the Leiden Algorithm

Considering that the MDEs usually co-occur and co-evolve within limited spatial scales, it is necessary to divide the YRB into several relatively independent subregions, where the MDEs may evolve more synchronously within these subregions. As undirected networks often exhibit distinct community structures, characterized by dense connections between nodes within the same community and relatively sparse connections between nodes in different communities, community detection has emerged as a promising approach for identifying such subregions [58]. Although a wide array of community detection algorithms are available at present, only a few are suitable for large networks containing hundreds of nodes. Among these algorithms, the Leiden algorithm was chosen to identify the MDE synchronized subregions in the YRB. This algorithm offers superior accuracy and robustness in detecting community structures within large networks and is an enhancement over the Louvain algorithm applied in previous studies [36,59]. The Leiden algorithm achieves the optimal partitioning by optimizing the modularity (*Mod*), which is defined by the following expression:

$$Mod = \frac{1}{2M}\sum_{i,j}\left[\left(A_{ij}^{Q} - \frac{k_i k_j}{2M}\right)\delta(S_i, S_j)\right] \tag{11}$$

where M is the total number of edges in the network; A_{ij}^{Q} is the element of the undirected adjacency matrix A^{Q}; k_i and k_j are the numbers of edges adjacent to nodes i and j, respectively (i.e., the degree of nodes i and j); S_i and S_j are the communities to which nodes i and j belong, respectively; $\delta(S_i, S_j)$ is 1 if nodes i and j belong to the same community and 0 otherwise. Higher modularity values indicate denser intracommunity links and sparser intercommunity links. This suggests that the network is effectively divided into distinct and non-overlapping communities, revealing meaningful association patterns between nodes within each community. By maximizing the modularity, the Leiden algorithm is capable of achieving a more effective partitioning of the network, enabling the identification of MDE synchronized subregions within the YRB.

3.6. Identification of MDE Representative Grids in MDE Synchronized Subregions by the $Z - P$ Space Approach

MDE occurrences in different MDE synchronized subregions in the YRB may be influenced by various teleconnection factors. To determine the regional discrepancies in influence effects from teleconnection factors, the linkages between teleconnection factors and representative SPEI series for individual subregions must be evaluated. In traditional terms, representative SPEI series are typically defined as the mean of all grids' SPEI series within the subregion. However, this conventional definition can lead to a reduction in variability and potentially obscure existing associations with teleconnection patterns [60]. In this study, grids with the highest number of intracommunity links in individual MDE synchronized subregions were considered to be representative due to their strong MDE synchronization [61]. Thus, their linkages to teleconnection factors were expected to have the highest similarity to those of the other grids within their respective subregions. The representative grid for each subregion was identified using the $Z - P$ space approach in this study, where Z is the within-module degree and P is the participation coefficient [62,63]. Z is a within-community version of DC and shows how well a node is connected to other nodes in the same community. It is estimated as follows:

$$Z_i = \frac{K_i - \overline{K_{S_i}}}{\sigma_{K_{S_i}}} \tag{12}$$

where K_i is the degree of node i in community S_i, $\overline{K_{S_i}}$ is the average degree of all nodes in community S_i, and $\sigma_{K_{S_i}}$ is the standard deviation of all degrees in S_i. Since two nodes with similar Z values may play different roles within the community, this measure is often combined with the participation coefficient P for a more comprehensive assessment of node representativeness.

The participation coefficient P_i compares the number of links of node i to nodes in all communities with the number of links within its own community. The P_i of node i is defined as follows:

$$P_i = 1 - \sum_{S_j=1}^{N_m} \left(\frac{k_{iS_j}}{k_i} \right)^2 \tag{13}$$

where N_m represents the number of communities in the network, k_{iS_j} is the number of links of node i to nodes in community S_j, and k_i is the degree of node i in the network. Essentially, P measures how uniformly a node's links are distributed among all of the communities. If a node's links are evenly spread across different communities, its p value is close to one. Conversely, if all of its links are confined within its own community, its p value is zero. The grid with the highest number of intracommunity links is designated as the MDE representative grid based on the argument that it shows the strongest MDE synchronization within the subregion [61].

3.7. Evaluation of MDE Teleconnection Patterns of MDE Synchronized Subregions by Wavelet Coherence Analysis (WCA)

To reveal the MDE teleconnection patterns of MDE synchronized subregions, wavelet coherence analysis (WCA) was performed on the teleconnection factors (ENSO, PDO, NAO, AO) and the SPEI-3 series of corresponding MDE representative grids. WCA enables the detection of variations in coherence and phase difference between two signals over time, and it is particularly well suited for capturing the linkages between hydroclimatological variables at multiple timescales [64,65]. The wavelet coherence between time series $X\{X_t\}$ and $Y\{Y_t\}$ was defined by Torrence and Compo [66] as follows:

$$R^2(s,t) = \frac{\left|\varsigma(s^{-1}W_{xy}(s,t)\right|}{\varsigma(s^{-1}|W_x(s,t)|^2)\varsigma(s^{-1}\left|W_y(s,t)\right|^2)} \tag{14}$$

where ζ is a smoothing operator and can be expressed as $\varsigma(W) = \varsigma_{\text{scale}}(\varsigma_{\text{time}}(W(s,t)))$, where ς_{scale} denotes smoothing along the wavelet scale axis and ς_{time} denotes smoothing over time. W_{xy} represents the cross-wavelet coefficient between X and Y. $W_x(s,t)$ and $W_y(s,t)$ denote the wavelet coefficients obtained from the wavelet transform of X and Y at scale s and time t, respectively.

Furthermore, the global wavelet coherence (GWC) at a certain scale s is defined as the time-averaged value of the wavelet coefficients at the scale with the cone of influence (COI) [65,67]. This is a useful measure to examine the common characteristic periodicities between X and Y, which are estimated by

$$R^2(s) = \frac{1}{n_s} \sum_{t=t_1}^{t_2} R^2(s,t) \tag{15}$$

where n_s is the number of points with the COI and $n_s = t_2 - t_1 + 1$. The GWC results are used to characterize the associations between MDEs in individual subregions and the four teleconnection factors at different timescales.

4. Results and Discussion

4.1. MDEs' Synchronized Structure over the YRB

The spatial distributions of the network-based metrics, including the DC, MSD, BC, and CC, obtained from the MDE synchronized network over the YRB, are presented in

Figures 4–7, respectively. Notably, the results of DC, BC, and CC were corrected for the boundary effect, as detailed in Figures 4, 6 and 7, respectively. The DC values in the peripheral zones were found to be obviously small before boundary effect correction (Figure 4a), and the boundary-affected DC values gradually increased from the peripheral zones to the internal zones of the YRB (Figure 4b). The reason that the DC values are higher in the internal zones is that the internal grids tend to have more short-distance neighbors, resulting in a higher probability of forming more connections in the surrogate networks. The boundary effect correction led to relatively higher corrected DC values compared to the uncorrected ones in the peripheral zones, demonstrating the effectiveness of the boundary effect correction (Figure 4c). Similar results were also found in previous studies [52,53,56]. According to the corrected DC result in Figure 4c, areas with relatively high DC values (>0.4) are mainly concentrated in the northeastern and northwestern parts, suggesting that a higher number of grids experience co-occurring MDEs in these zones. In contrast, areas with low DC values (<0.1) are prevalent in the upper reaches, suggesting that these areas have a low level of synchronization with other grids in terms of MDE occurrences. The spatial distribution of the DC results is consistent with that calculated by Gao et al. [39].

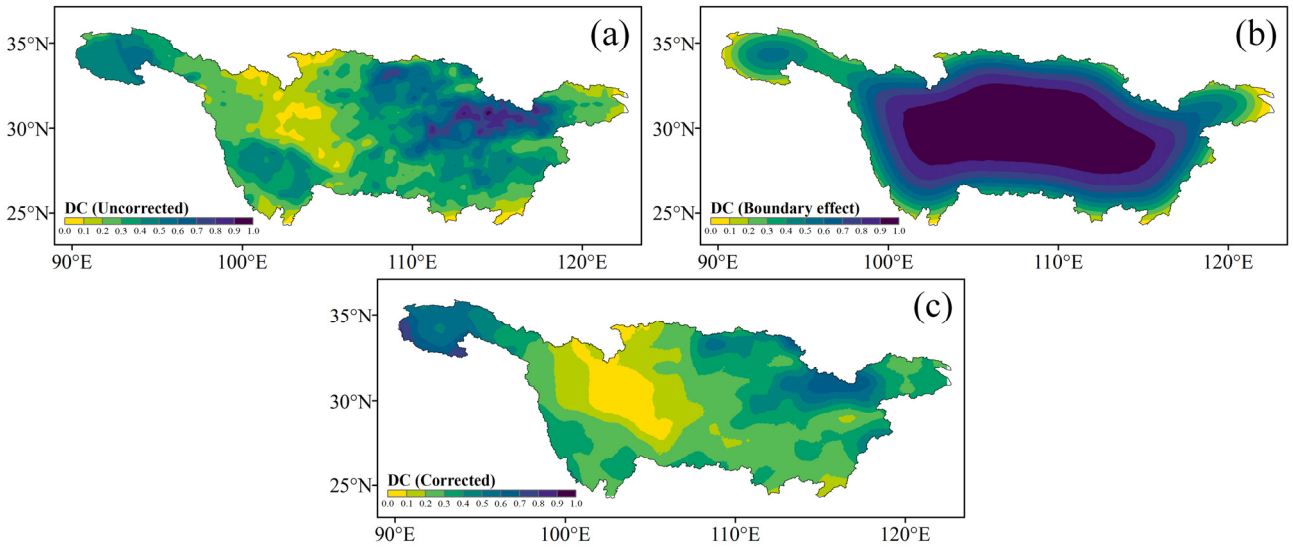


Figure 4. Spatial distributions of (**a**) uncorrected degree centrality (DC) values obtained from the original MDE synchronized network over the YRB, (**b**) boundary-affected DC values obtained from 100 surrogate networks, and (**c**) corrected DC values calculated by dividing the uncorrected DC values by the boundary-affected DC values.

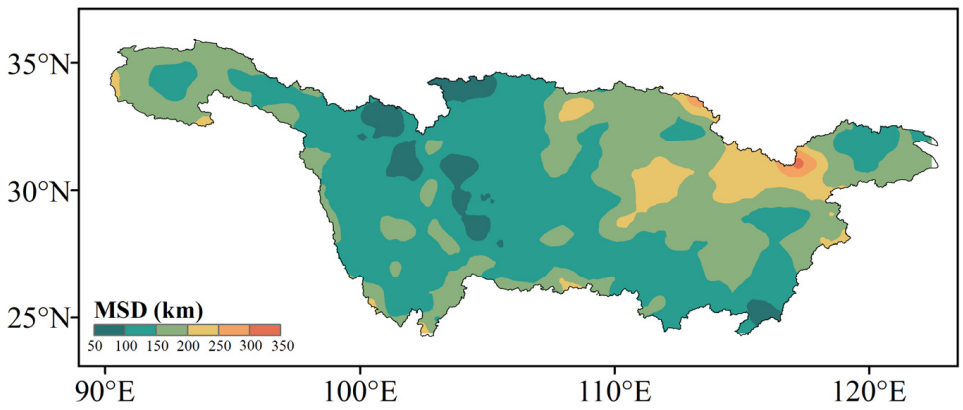


Figure 5. Spatial distribution of mean synchronized distance (MSD) obtained from the MDE synchronized network over the YRB.

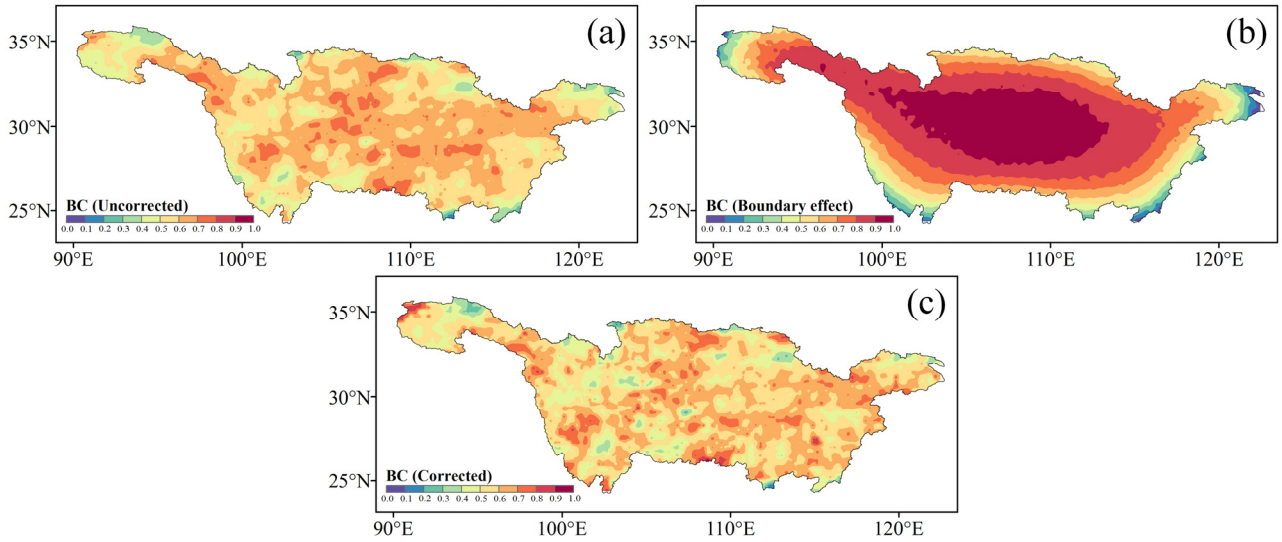


Figure 6. Spatial distributions of (**a**) uncorrected betweenness centrality (BC) obtained from the original MDE synchronized network over the YRB, (**b**) boundary-affected BC obtained from 100 surrogate networks, and (**c**) corrected BC calculated by dividing the uncorrected BC values by the boundary-affected BC values.

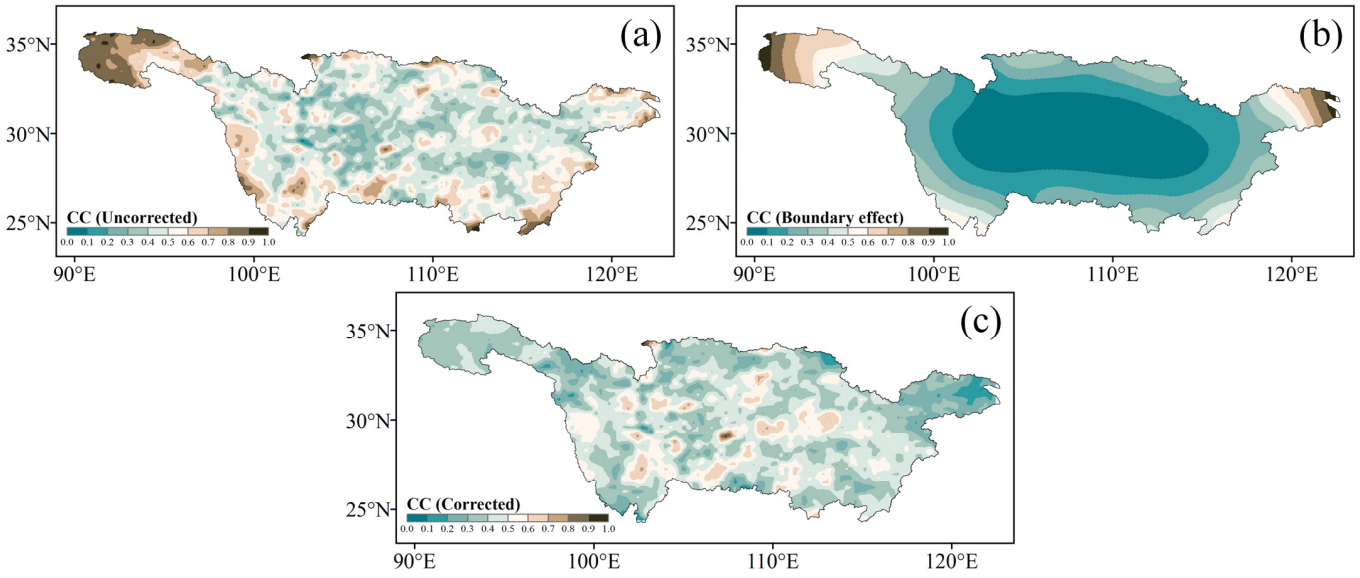


Figure 7. Spatial distributions of (**a**) uncorrected clustering coefficient (CC) obtained from the original MDE synchronized network over the YRB, (**b**) boundary-affected CC obtained from 100 surrogate networks, and (**c**) corrected CC calculated by dividing the uncorrected CC values by the boundary-affected CC values.

The spatial distribution of the MSD results (Figure 5) exhibited an evident correlation with the corrected DC results, which is also similar to the findings of previous studies [52,53,56]. The areas characterized by high DC values in the northeast also exhibited larger MSD values, exceeding 200 km. This observation suggests a propensity for MDE occurrences with a broader spatial scale in these areas. In contrast, certain areas characterized by low DC values featured MSD values below 100 km, indicating a higher likelihood of localized MDEs within these areas. Although the results of DC and MSD are consistent, their meanings are not the same. DC focuses on the geographic area of MDE synchronization, while MSD indicates the geographic distance of MDE synchronization. The coupling of DC and MSD results for a grid can effectively reveal its spatial scale of

MDE synchronization. The MDE synchronized scale of each grid is usually limited to a certain range, demonstrating the regionality of MDEs' occurrence and evolution over the YRB. Consequently, it becomes imperative to partition synchronized subregions where MDEs are more susceptible to occurrence and evolution within the YRB.

The spatial distributions of the BC results are presented in Figure 6. Similar to the boundary-affected DC results, the boundary-effected BC results in Figure 6b show an increase from the peripheral zones to the internal zones, resulting in relatively higher corrected BC values compared to the uncorrected ones in the peripheral zones, as well as lower corrected BC values than the uncorrected ones in the internal zones, as illustrated in Figure 6c. Figure 6c demonstrates that there are two main pathways for the propagation of synchronous MDEs in the basin, which are characterized by high BC values. The first pathway is a central path traversing the southwestern and central parts of the YRB along a northeast–southwest direction. The second pathway is an eastern path crossing the southern and northeastern parts of the YRB along a northeast–southwest direction. These two pathways signify the prevailing tendency of the climatic factors responsible for driving MDEs.

The spatial distributions of the CC results are presented in Figure 7. In contrast to the boundary-affected DC and BC results, the boundary-affected CC results in Figure 7b exhibit a gradual decrease from the peripheral zones to the internal zones of the YRB. This results in relatively lower corrected BC values compared to the uncorrected ones in the peripheral zones, and higher corrected BC values than the uncorrected ones in the internal zones, as illustrated in Figure 7c. Notably, the boundary results of DC, BC, and CC align with findings from previous studies, as determined by their definitions [53,56]. In accordance with the CC results reported by Mondal et al. [51], Figure 7c reveals a negative correlation between CC and BC. Areas characterized by higher CC values typically exhibit lower BC values, implying that these areas experience stronger MDE spatial coherence but have relatively weaker potential for MDE propagation.

4.2. Synchronized Subregions and Representative Grids of MDEs within the YRB

The spatial distribution of MDE synchronized subregions in the YRB is shown in Figure 8. A total of eight subregions were identified in the YRB. Subregions 1, 2, and 3 are located in the southern part of the basin, while the remaining subregions are located in the northern part of the basin. The overall distribution of individual subregions was close to that identified by Huang et al. [43], but two additional subregions were identified in this study, i.e., Subregions 6 and 7. This difference verifies the superior sensitivity of the Leiden algorithm in regional partitioning. The points marked in Figure 4 represent the positions of identified MDE representative grids in individual subregions. The spatial ranges of individual subregions are generally consistent with the MDE spatial scales identified by the DC and MSD results, which means that most grids within these subregions possess similar DC and MSD values and are more likely to experience synchronous MDEs. For instance, the grids with the highest DC and MSD values are mainly distributed in Subregion 4, which possesses the greatest area, while grids with the lowest DC and MSD values are predominantly found in Subregion 7, which covers the smallest area.

4.3. MDE Characteristics of MDE Synchronized Subregions

The spatial distributions of MDEs' frequency, duration, total severity, and peak over the YRB are shown in Figure 9. These results were found to be similar to those calculated by Gao et al. [39]. Areas with higher MDE frequency are mainly observed in the upper and lower reaches of the YRB, while fewer MDEs occur in the lower reaches (Figure 9a). Subregion-specific statistics of MDE frequency are presented in Table 2, revealing that Subregion 3 experiences the lowest number of MDEs, likely attributable to the relatively infrequent occurrence of drought-inducing weather systems in this subregion. The spatial patterns of MDE duration and total severity are almost opposite to that of MDE frequency in this basin (Figure 9b,c). It should be noted that the northwest of Subregion 1 has the

lowest MDE frequency but experiences the longest duration and the most serious severity of MDEs. This leads to Subregion 1 having the highest MDE duration value and the lowest MDE total severity value, as outlined in Table 2. Regarding the MDE peak values (Figure 9d), a few locations within Subregions 3, 5, 6, and 7 exhibit low peaks, contributing to the relatively low MDE peak of these subregions, as detailed in Table 2. Overall, the MDE characteristics vary significantly across the YRB.

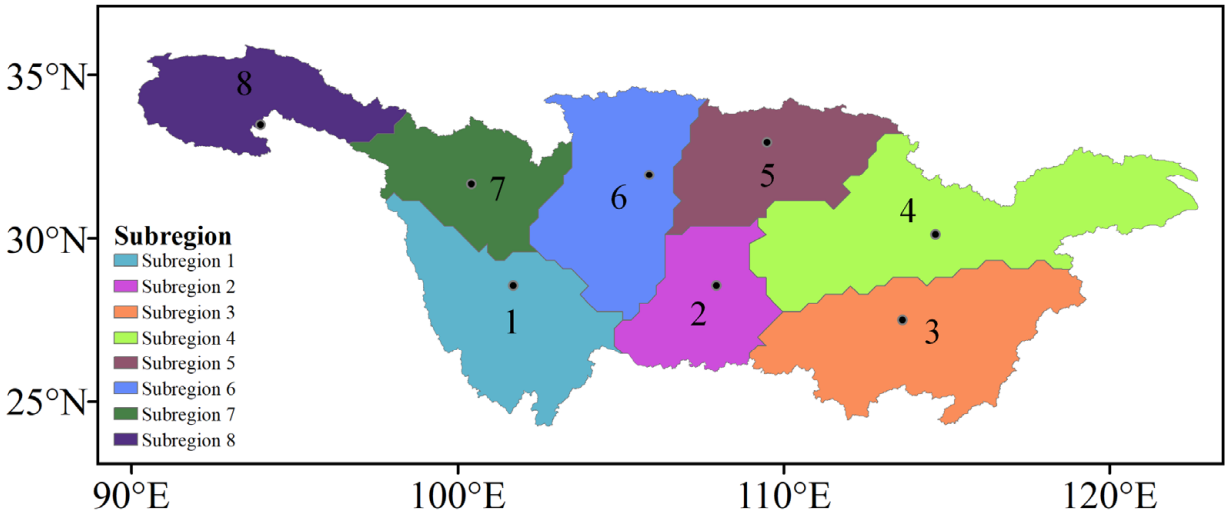


Figure 8. Spatial distribution of MDE synchronized subregions and MDE representative grids over the YRB.

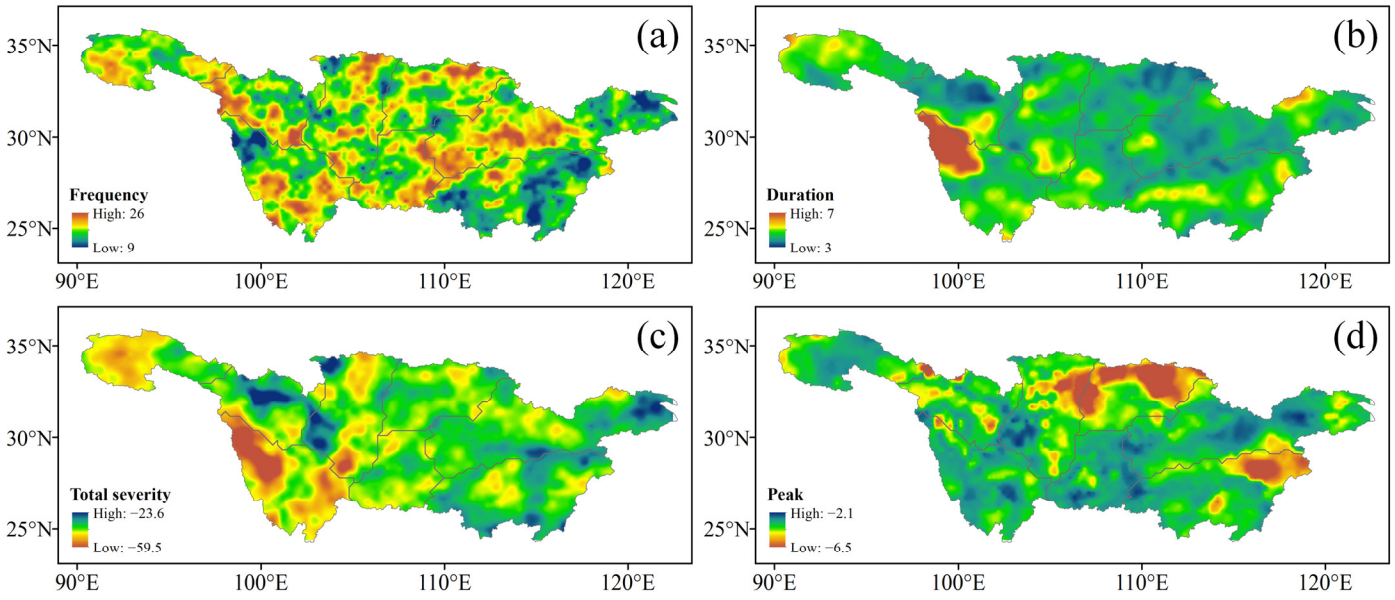


Figure 9. Spatial distributions of (**a**) frequency, (**b**) duration, (**c**) total severity, and (**d**) peak for grid-based MDEs over the YRB during 1961–2021.

The occurrence months of MDEs were counted for all grids within the individual subregions, and the subregion-averaged frequency distributions at the temporal scale are shown in Figure 10. The variations in the monthly MDE occurrence distributions across different subregions are apparent, which is the outcome of diverse climatic patterns driving MDEs in each subregion. This indicates that different climatic factors may influence water vapor transport and the convergence of cold and warm air masses in each subregion during distinct periods, leading to variations in the frequencies of MDEs. In Subregions 1–7,

the season with the highest frequency of MDEs gradually shifts from winter (December, January, and February) to summer (June, July, and August), while Subregion 8 exhibits greater month-to-month frequency fluctuations. In Subregions 1 and 2, February stands out as the month with the highest MDE frequency, followed by increased frequency in the summer months. Subregion 2, in particular, displays more pronounced variations. Although Subregions 3 and 4 are both situated in the middle and lower reaches of the YRB, they feature distinct temporal frequency distributions of MDEs. In Subregion 3, May and June experience the highest MDE frequencies, while Subregion 4 sees increased MDE frequency in June and July, with a notable divergence in March between the two subregions. Subregion 5 demonstrates a relatively high and stable MDE frequency, fluctuating only slightly from March to September. Subregion 6 exhibits substantial month-to-month variations in MDE frequency, with distribution patterns akin to those of Subregion 8. Finally, the MDEs in Subregion 7 are primarily concentrated in July and August, with lower frequencies observed in other months.

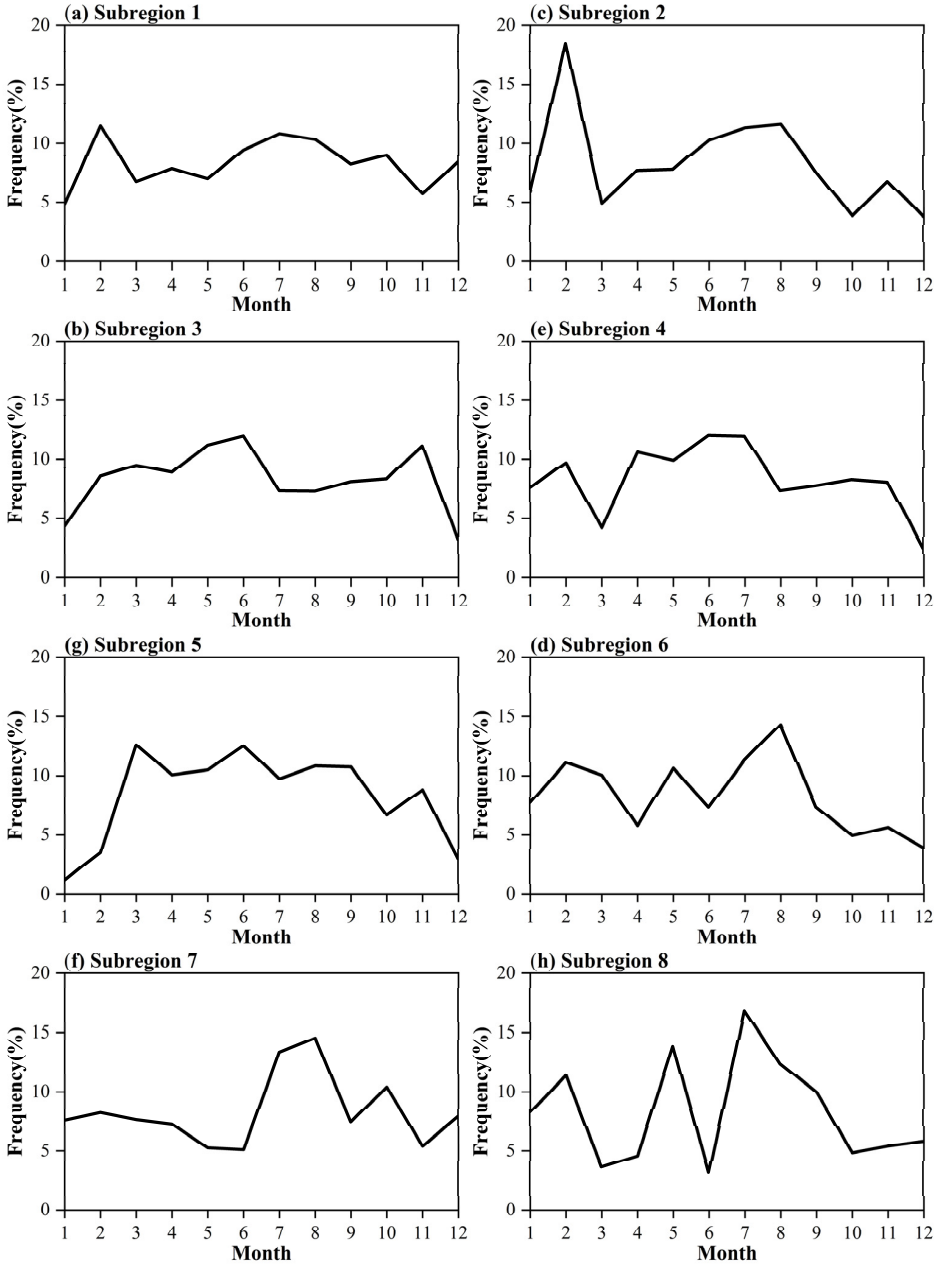


Figure 10. Monthly frequency distributions of MDEs in all of the MDE synchronized subregions.

Table 2. Characteristics of area-averaged MDEs in the MDE synchronized subregions.

Subregion	Frequency	Duration	Total Severity	Peak
1	17.8	4.4	−44.1	−2.6
2	18.3	3.9	−38.8	−2.5
3	16.1	3.9	−36.3	−2.8
4	17.8	3.8	−36.5	−2.6
5	18.1	3.7	−38.2	−3.4
6	17.8	3.9	−38.5	−2.9
7	18.2	3.8	−36.5	−2.8
8	18.0	4.0	−41.2	−2.6

4.4. MDE Teleconnection Patterns of MDE Synchronized Subregions

The GWC results between the four teleconnection factors (ENSO, PDO, NAO, and AO) and the SPEI-3 series of MDE representative grids in individual subregions at multiple timescales are depicted in Figure 11, where the highlighted red parts represent timescales with a 95% confidence level. Figure 11a illustrates a significant association between ENSO and MDEs in all subregions, particularly at timescales of less than one year. This suggests that the YRB exhibits variable lagged responses to previous ENSO events occurring several months prior. Specifically, Subregions 1, 3, 4, and 5 exhibit significant responses within half a year, while other subregions display significant responses within six months to one year. Subregions 2, 3, and 6 also show significant responses at timescales of 1–2 years, while Subregions 1, 4, and 8 exhibit significant responses at timescales of 2–4 years. Remarkably, only Subregions 1 and 3 demonstrate significant response periods exceeding 4 years, occurring in the range of 8–16 years.

Compared with ENSO, there are weaker associations between the other three teleconnection factors and MDEs in each subregion shown in Figure 11b–d, indicating relatively weaker influence effects from these factors. Figure 11b indicates that aside from Subregion 3, the PDO exhibits a significant association with the remaining subregions. Subregions 5, 6, and 8 display single significant response periods, situated within timescales of 4–8, 0.25–0.5, and 4–8 years, respectively. Subregion 2's significant response period spans 0.5 to 2 years, while Subregions 1, 4, and 7 exhibit both short response periods (i.e., less than half a year) and longer ones (i.e., more than 2 years). Figure 11c shows that the NAO does not significantly influence Subregions 5, 6, and 8. Subregions 4 and 7 feature solitary significant response periods, falling within timescales of 8–16 and 0.5–1 years, respectively. Subregions 1, 2, and 3, located in the southern part of the YRB, exhibit multiple significant response periods across various timescales. Subregion 1 displays a timescale of less than 2 years, Subregion 2 shows significant response periods of around 0.25–0.5 years and approximately 8 years, and Subregion 3 demonstrates significant response periods mainly within 1 to 2 years. Lastly, Figure 11d demonstrates that the AO does not significantly influence Subregions 7 and 8. Subregions 3 and 6 each have a single significant response period to the AO, both within the timescale of 0.25 to 0.5 years. Subregions 1, 2, 4, and 5 exhibit significant response periods of less than half a year. Subregion 2 additionally features response periods within 0.5–1 and 2–4 years, while Subregions 4 and 5 show significant response periods of 8–16 years. In summary, compared to other factors, ENSO exerts the greatest influence on MDEs within the individual subregions; the NAO has a significant influence on the southern subregions of the YRB (Subregions 1, 2, and 3), while the AO has a significant influence on the northern subregions of the YRB (Subregions 4, 5, and 6).

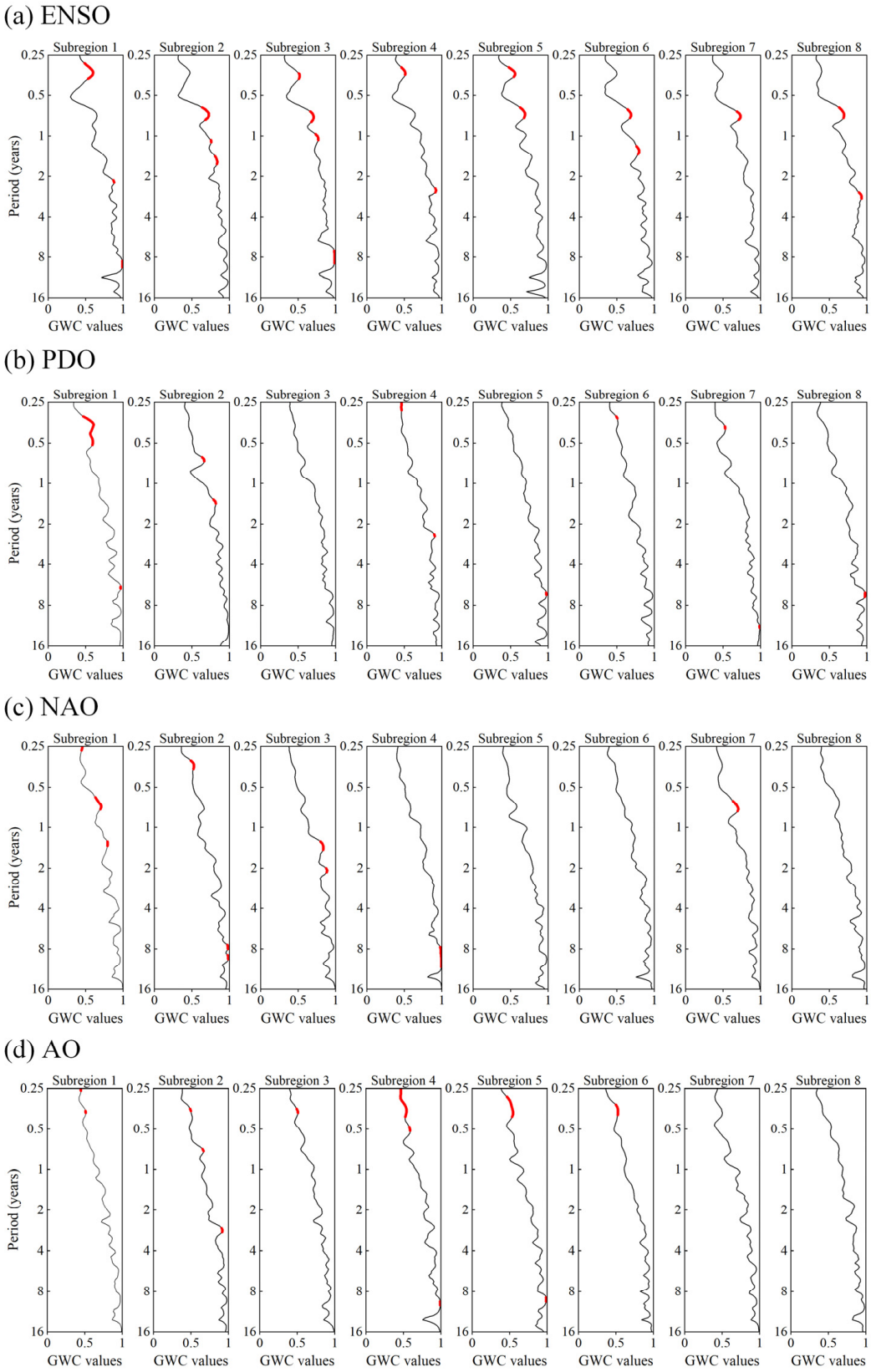


Figure 11. Global wavelet coherence (GWC) results between four teleconnection factors (ENSO, PDO, NAO, and AO) and the SPEI-3 series of MDE representative grids within all of the MDE synchronized subregions. GWC values are shown as black lines, and significant influences (at the 95% significance level) are marked in red.

5. Conclusions

This study utilized a complex network-based methodology to construct the MDE synchronized network over the YRB based on the extracted grid-based MDE occurrence sequences. The analysis of this network provided key insights into various spatial aspects of MDEs' evolution in the YRB, including the MDEs' topological structure, synchronized subregions, and representative grids. This study further investigated the MDE characteristics and MDE teleconnection patterns of individual subregions. By quantifying the MDEs' synchronized structure and teleconnection patterns at the basin scale, this study provides a potential foundation to develop sea-surface temperature anomaly (SSTA)-based drought prediction models, which can contribute to enhanced drought forecasting and resilience strategies. The main conclusions of this study can be summarized as follows:

- The northeastern portion of the YRB exhibits significant MDE synchronization, as evidenced by its high DC and MSD values. These characteristics make this region more susceptible to experiencing widespread MDEs. Conversely, specific areas in the upper reaches, characterized by low DC and MSD values, suggest a higher likelihood of localized MDE occurrences. The BC results highlight the propagation of synchronous MDEs along two main pathways: the central pathway and the eastern pathway. These two pathways display relatively low MDE spatial coherence, as indicated by the low CC values.
- The YRB is partitioned into eight MDE synchronized subregions, and the spatial ranges of the individual subregions are consistent with the MDE synchronized scales identified from the DC and MSD results. Each subregion exhibits distinct characteristics in terms of the frequency, duration, total severity, and peak of MDEs, as well as distinct MDE temporal frequency distributions. Among these subregions, Subregion 3 in the southeast experiences the fewest MDEs, while Subregion 1 in the southwest has the highest MDE duration value and the strongest MDE total severity value. Additionally, Subregions 3, 5, 6, and 7 in the southeast and north show relatively low MDE peak values. In Subregions 1–7, the season with the highest MDE frequency gradually shifts from winter to summer, while Subregion 8 in the northwest exhibits greater month-to-month fluctuations in the MDEs' temporal frequency.
- The MDE synchronized subregions exhibit significant variability in MDE teleconnection patterns at multiple timescales. ENSO exerts a strong influence on MDEs in all subregions, whereas the influence effects from other teleconnection factors (i.e., the PDO, NAO, and AO) are relatively weaker. Specifically, the PDO shows a significant association with MDEs in all subregions except for Subregion 3 in the southeast, the NAO displays a significant influence on the MDEs in the southern subregions of the YRB (Subregions 1, 2, and 3), and the AO has a more pronounced influence on the MDEs in the northern subregions of the YRB (Subregions 4, 5, and 6).

Author Contributions: Supervision, D.Z.; funding acquisition, Z.Z.; conceptualization, S.Z.; methodology, L.L.; software, L.L.; writing—original draft, L.L.; writing—review and editing, L.L., C.G. and X.T.; visualization, C.G. All authors have read and agreed to the published version of the manuscript.

Funding: This research was funded by the Open Research Fund of Hubei Key Laboratory of Intelligent Yangtze and Hydroelectric Science, China Yangtze Power Co., Ltd. (grant number ZH2002000109), the Science and Technology Planning Project of Guangdong Province (grant number 2020B1212030005), and the Basic and Applied Basic Research Foundation of Guangdong Province (grant number 2021A1515110410 and 2023A1515010972).

Data Availability Statement: The data presented in this study are available upon request from the corresponding author. The data are not publicly available due to the data sharing policy.

Conflicts of Interest: The authors declare no conflict of interest.

References

1. Sheffield, J.; Wood, E.F.; Roderick, M.L. Little Change in Global Drought over the Past 60 Years. *Nature* **2012**, *491*, 435–438. [CrossRef] [PubMed]
2. Trenberth, K.E.; Dai, A.; Van der Schrier, G.; Jones, P.D.; Barichivich, J.; Briffa, K.R.; Sheffield, J. Global Warming and Changes in Drought. *Nat. Clim. Chang.* **2014**, *4*, 17–22. [CrossRef]
3. Zhao, R.; Sun, H.; Xing, L.; Li, R.; Li, M. Effects of Anthropogenic Climate Change on the Drought Characteristics in China: From Frequency, Duration, Intensity, and Affected Area. *J. Hydrol.* **2023**, *617*, 129008. [CrossRef]
4. Gudmundsson, L.; Boulange, J.; Do, H.X.; Gosling, S.N.; Grillakis, M.G.; Koutroulis, A.G.; Leonard, M.; Liu, J.; Schmied, H.M.; Papadimitriou, L.; et al. Globally Observed Trends in Mean and Extreme River Flow Attributed to Climate Change. *Science* **2021**, *371*, 1159–1162. [CrossRef]
5. Min, S.-K.; Zhang, X.; Zwiers, F.W.; Hegerl, G.C. Human Contribution to More-Intense Precipitation Extremes. *Nature* **2011**, *470*, 378–381. [CrossRef]
6. Foroumandi, E.; Nourani, V.; Huang, J.J.; Moradkhani, H. Drought Monitoring by Downscaling GRACE-Derived Terrestrial Water Storage Anomalies: A Deep Learning Approach. *J. Hydrol.* **2023**, *616*, 128838. [CrossRef]
7. Foroumandi, E.; Nourani, V.; Kantoush, S.A. Investigating the Main Reasons for the Tragedy of Large Saline Lakes: Drought, Climate Change, or Anthropogenic Activities? A Call to Action. *J. Arid. Environ.* **2022**, *196*, 104652. [CrossRef]
8. Bevacqua, E.; Zappa, G.; Lehner, F.; Zscheischler, J. Precipitation Trends Determine Future Occurrences of Compound Hot–Dry Events. *Nat. Clim. Chang.* **2022**, *12*, 350–355. [CrossRef]
9. Mukherjee, S.; Mishra, A.K. Increase in Compound Drought and Heatwaves in a Warming World. *Geophys. Res. Lett.* **2021**, *48*, e2020GL090617. [CrossRef]
10. Zscheischler, J.; Seneviratne, S.I. Dependence of Drivers Affects Risks Associated with Compound Events. *Sci. Adv.* **2017**, *3*, e1700263. [CrossRef]
11. Zscheischler, J.; Westra, S.; Van den Hurk, B.J.J.M.; Seneviratne, S.I.; Ward, P.J.; Pitman, A.; AghaKouchak, A.; Bresch, D.N.; Leonard, M.; Wahl, T.; et al. Future Climate Risk from Compound Events. *Nat. Clim. Chang.* **2018**, *8*, 469–477. [CrossRef]
12. Singh, J.; Ashfaq, M.; Skinner, C.; Anderson, W.; Singh, D. Amplified Risk of Spatially Compounding Droughts during Co-Occurrences of Modes of Natural Ocean Variability. *NPJ Clim. Atmos. Sci.* **2021**, *4*, 7. [CrossRef]
13. Xia, J.; Chen, J.; She, D.X. Impacts and Countermeasures of Extreme Drought in the Yangtze River Basin in 2022. *J. Hydraul. Eng.* **2022**, *53*, 1143–1153. [CrossRef]
14. Blöschl, G.; Bierkens, M.F.; Chambel, A.; Cudennec, C.; Destouni, G.; Fiori, A.; Kirchner, J.W.; McDonnell, J.J.; Savenije, H.H.; Sivapalan, M.; et al. Twenty-Three Unsolved Problems in Hydrology (UPH)—A Community Perspective. *Hydrol. Sci. J.* **2019**, *64*, 1141–1158. [CrossRef]
15. Wen, X.; Tu, Y.; Tan, Q.; Li, W.; Fang, G.; Ding, Z.; Wang, Z. Construction of 3D Drought Structures of Meteorological Drought Events and Their Spatio-Temporal Evolution Characteristics. *J. Hydrol.* **2020**, *590*, 125539. [CrossRef]
16. Apurv, T.; Cai, X. Drought Propagation in Contiguous U.S. Watersheds: A Process-Based Understanding of the Role of Climate and Watershed Properties. *Water Resour. Res.* **2020**, *56*, e2020WR027755. [CrossRef]
17. Herrera-Estrada, J.E.; Satoh, Y.; Sheffield, J. Spatiotemporal Dynamics of Global Drought. *Geophys. Res. Lett.* **2017**, *44*, 2254–2263. [CrossRef]
18. Konapala, G.; Mishra, A. Review of Complex Networks Application in Hydroclimatic Extremes with an Implementation to Characterize Spatio-Temporal Drought Propagation in Continental USA. *J. Hydrol.* **2017**, *555*, 600–620. [CrossRef]
19. Rajsekhar, D.; Singh, V.P.; Mishra, A.K. Multivariate Drought Index: An Information Theory Based Approach for Integrated Drought Assessment. *J. Hydrol.* **2015**, *526*, 164–182. [CrossRef]
20. Vicente-Serrano, S.M.; Peña-Angulo, D.; Murphy, C.; López-Moreno, J.I.; Tomas-Burguera, M.; Dominguez-Castro, F.; Tian, F.; Eklundh, L.; Cai, Z.; Alvarez-Farizo, B.; et al. The Complex Multi-Sectoral Impacts of Drought: Evidence from a Mountainous Basin in the Central Spanish Pyrenees. *Sci. Total Environ.* **2021**, *769*, 144702. [CrossRef]
21. Zhang, X.; Hao, Z.; Singh, V.P.; Zhang, Y.; Feng, S.; Xu, Y.; Hao, F. Drought Propagation under Global Warming: Characteristics, Approaches, Processes, and Controlling Factors. *Sci. Total Environ.* **2022**, *838*, 156021. [CrossRef] [PubMed]
22. Wang, D.; Hejazi, M.; Cai, X.; Valocchi, A.J. Climate Change Impact on Meteorological, Agricultural, and Hydrological Drought in Central Illinois. *Water Resour. Res.* **2011**, *47*, W09527. [CrossRef]
23. Li, L.; Zhao, L.; Ge, J.; Yang, P.; Wu, F. Investigating Drought Propagation Time, Relationship, and Drivers in Perennial River Basins of China. *Water* **2022**, *14*, 2812. [CrossRef]
24. Zhu, K.; Xu, Y.; Lu, F.; Sun, X.; Gao, M.; Han, X.; Li, D.; Jiang, M. Spatio-Temporal Evolution and Propagation of Meteoro-Hydrological Drought in Yalong River Basin. *Water* **2023**, *15*, 1025. [CrossRef]
25. Vicente-Serrano, S.M.; Begueria, S.; Lopez-Moreno, J.I. A Multiscalar Drought Index Sensitive to Global Warming: The Standardized Precipitation Evapotranspiration Index. *J. Clim.* **2010**, *23*, 1696–1718. [CrossRef]
26. Palmer, W.C. *Meteorological Drought*; US Department of Commerce, Weather Bureau: Washington, DC, USA, 1965; Volume 30.
27. Liu, Q.; Zhang, S.; Zhang, H.; Bai, Y.; Zhang, J. Monitoring Drought Using Composite Drought Indices Based on Remote Sensing. *Sci. Total Environ.* **2020**, *711*, 134585. [CrossRef]
28. Gocic, M.; Trajkovic, S. Spatiotemporal Characteristics of Drought in Serbia. *J. Hydrol.* **2014**, *510*, 110–123. [CrossRef]
29. Mishra, A.K.; Singh, V.P. A Review of Drought Concepts. *J. Hydrol.* **2010**, *391*, 202–216. [CrossRef]

30. Wu, J.; Chen, X. Spatiotemporal Trends of Dryness/Wetness Duration and Severity: The Respective Contribution of Precipitation and Temperature. *Atmos. Res.* **2019**, *216*, 176–185. [CrossRef]
31. Gonzalez-Hidalgo, J.; Vicente-Serrano, S.; Pena-Angulo, D.; Salinas, C.; Tomas-Burguera, M.; Begueria, S. High-Resolution Spatio-Temporal Analyses of Drought Episodes in the Western Mediterranean Basin (Spanish Mainland, Iberian Peninsula). *Acta Geophys.* **2018**, *66*, 381–392. [CrossRef]
32. Huang, S.; Zhang, X.; Chen, N.; Li, B.; Ma, H.; Xu, L.; Li, R.; Niyogi, D. Drought Propagation Modification after the Construction of the Three Gorges Dam in the Yangtze River Basin. *J. Hydrol.* **2021**, *603*, 127138. [CrossRef]
33. Tijdeman, E.; Blauhut, V.; Stoelzle, M.; Menzel, L.; Stahl, K. Different Drought Types and the Spatial Variability in Their Hazard, Impact, and Propagation Characteristics. *Nat. Hazards Earth Syst. Sci.* **2022**, *22*, 2099–2116. [CrossRef]
34. Palazzolo, N.; Peres, D.J.; Bonaccorso, B.; Cancelliere, A. A Probabilistic Analysis of Drought Areal Extent Using SPEI-Based Severity-Area-Frequency Curves and Reanalysis Data. *Water* **2023**, *15*, 3141. [CrossRef]
35. Mondal, S.; Mishra, A.; Leung, R.; Cook, B. Global Droughts Connected by Linkages between Drought Hubs. *Nat. Commun.* **2023**, *14*, 144. [CrossRef] [PubMed]
36. Konapala, G.; Mondal, S.; Mishra, A. Quantifying Spatial Drought Propagation Potential in North America Using Complex Network Theory. *Water Resour. Res.* **2022**, *58*, e2021WR030914. [CrossRef]
37. Fan, J.; Meng, J.; Ludescher, J.; Chen, X.; Ashkenazy, Y.; Kurths, J.; Havlin, S.; Schellnhuber, H. Statistical Physics Approaches to the Complex Earth System. *Phys. Rep.* **2021**, *896*, 1–84. [CrossRef] [PubMed]
38. Jha, V.; Gujrati, A.; Singh, R. Complex Network Theoretic Assessment of Precipitation-Driven Meteorological Drought in India: Past and Future. *Int. J. Climatol.* **2022**, *42*, 3274–3289. [CrossRef]
39. Gao, C.; Liu, L.; Zhang, S.; Xu, Y.-P.; Wang, X.; Tang, X. Spatiotemporal Patterns and Propagation Mechanism of Meteorological Droughts over Yangtze River Basin and Pearl River Basin Based on Complex Network Theory. *Atmos. Res.* **2023**, *292*, 106874. [CrossRef]
40. Birkinshaw, S.J.; Guerreiro, S.B.; Nicholson, A.; Liang, Q.; Quinn, P.; Zhang, L.; He, B.; Yin, J.; Fowler, H.J. Climate Change Impacts on Yangtze River Discharge at the Three Gorges Dam. *Hydrol. Earth Syst. Sci.* **2017**, *21*, 1911–1927. [CrossRef]
41. Sun, F.; Mejia, A.; Zeng, P.; Che, Y. Projecting Meteorological, Hydrological and Agricultural Droughts for the Yangtze River Basin. *Sci. Total Environ.* **2019**, *696*, 134076. [CrossRef]
42. Chen, J.; Wan, S.; Henebry, G.; Qi, J.; Gutman, G.; Sun, G.; Kappas, M. (Eds.) *Dryland East Asia: Land Dynamics amid Social and Climate Change*; Walter de Gruyter: Berlin, Germany, 2013.
43. Huang, T.; Xu, L.; Fan, H. Drought Characteristics and Its Response to the Global Climate Variability in the Yangtze River Basin, China. *Water* **2018**, *11*, 13. [CrossRef]
44. Yu, J.; Zhou, H.; Huang, J.; Yuan, Y. Prediction of Multi-Scale Meteorological Drought Characteristics over the Yangtze River Basin Based on CMIP6. *Water* **2022**, *14*, 2996. [CrossRef]
45. Tian, F.; Yang, J.; Liu, L.; Wu, J. Progress of Research on the Conception, Characteristic, and Influencing Factors of Drought Propagation from the Perspective of Geographic Sciences. *Prog. Geogr.* **2022**, *548*, 202–205. [CrossRef]
46. Wu, J.; Gao, X. A gridded daily observation dataset over China region and comparison with the other datasets. *Chin. J. Geophys.* **2013**, *56*, 1102–1111. [CrossRef]
47. Yang, J.; Chang, J.; Wang, Y.; Li, Y.; Hu, H.; Chen, Y.; Huang, Q.; Yao, J. Comprehensive Drought Characteristics Analysis Based on a Nonlinear Multivariate Drought Index. *J. Hydrol.* **2018**, *557*, 651–667. [CrossRef]
48. Zeng, P.; Sun, F.; Liu, Y.; Wang, Y.; Li, G.; Che, Y. Mapping Future Droughts under Global Warming across China: A Combined Multi-Timescale Meteorological Drought Index and SOM-Kmeans Approach. *Weather. Clim. Extrem.* **2021**, *31*, 100304. [CrossRef]
49. Quiroga, R.Q.; Kreuz, T.; Grassberger, P. Event Synchronization: A Simple and Fast Method to Measure Synchronicity and Time Delay Patterns. *Phys. Rev. E* **2002**, *66*, 041904. [CrossRef]
50. Agarwal, A.; Marwan, N.; Maheswaran, R.; Ozturk, U.; Kurths, J.; Merz, B. Optimal Design of Hydrometric Station Networks Based on Complex Network Analysis. *Hydrol. Earth Syst. Sci.* **2020**, *24*, 2235–2251. [CrossRef]
51. Wiedermann, M.; Donges, J.F.; Kurths, J.; Donner, R.V. Mapping and Discrimination of Networks in the Complexity-Entropy Plane. *Phys. Rev. E* **2017**, *96*, 042304. [CrossRef]
52. Boers, N.; Bookhagen, B.; Marwan, N.; Kurths, J.; Marengo, J. Complex Networks Identify Spatial Patterns of Extreme Rainfall Events of the South American Monsoon System. *Geophys. Res. Lett.* **2013**, *40*, 4386–4392. [CrossRef]
53. Mondal, S.; Mishra, A.K.; Leung, L.R. Spatiotemporal Characteristics and Propagation of Summer Extreme Precipitation Events over United States: A Complex Network Analysis. *Geophys. Res. Lett.* **2020**, *47*, e2020GL088185. [CrossRef]
54. Malik, N.; Bookhagen, B.; Marwan, N.; Kurths, J. Analysis of Spatial and Temporal Extreme Monsoonal Rainfall over South Asia Using Complex Networks. *Clim. Dyn.* **2012**, *39*, 971–987. [CrossRef]
55. Barnett, L.; Di Paolo, E.; Bullock, S. Spatially Embedded Random Networks. *Phys. Rev. E* **2007**, *76*, 056115. [CrossRef] [PubMed]
56. Rheinwalt, A.; Marwan, N.; Kurths, J.; Werner, P.; Gerstengarbe, F.-W. Boundary Effects in Network Measures of Spatially Embedded Networks. In Proceedings of the 2012 SC Companion: High Performance Computing, Networking Storage and Analysis, Salt Lake City, UT, USA, 10–16 November 2012; IEEE: Piscataway, NJ, USA, 2012; pp. 500–505.
57. Wiedermann, M.; Donges, J.F.; Kurths, J.; Donner, R.V. Spatial Network Surrogates for Disentangling Complex System Structure from Spatial Embedding of Nodes. *Phys. Rev. E* **2016**, *93*, 042308. [CrossRef]
58. Fortunato, S.; Hric, D. Community Detection in Networks: A User Guide. *Phys. Rep.* **2016**, *659*, 1–44. [CrossRef]

59. Traag, V.A.; Waltman, L.; Van Eck, N.J. From Louvain to Leiden: Guaranteeing Well-Connected Communities. *Sci. Rep.* **2019**, *9*, 5233. [CrossRef]
60. Kurths, J.; Agarwal, A.; Shukla, R.; Marwan, N.; Rathinasamy, M.; Caesar, L.; Krishnan, R.; Merz, B. Unravelling the Spatial Diversity of Indian Precipitation Teleconnections via a Non-Linear Multi-Scale Approach. *Nonlinear Process. Geophys.* **2019**, *26*, 251–266. [CrossRef]
61. Halverson, M.; Fleming, S. Complex Network Theory, Streamflow, and Hydrometric Monitoring System Design. *Hydrol. Earth Syst. Sci.* **2015**, *19*, 3301–3318. [CrossRef]
62. Agarwal, A.; Marwan, N.; Maheswaran, R.; Merz, B.; Kurths, J. Quantifying the Roles of Single Stations within Homogeneous Regions Using Complex Network Analysis. *J. Hydrol.* **2018**, *563*, 802–810. [CrossRef]
63. Guimera, R.; Amaral, L.A.N. Cartography of Complex Networks: Modules and Universal Roles. *J. Stat. Mech. Theory Exp.* **2005**, *2005*, P02001. [CrossRef]
64. Peters, D.P.; Pielke Sr, R.A.; Bestelmeyer, B.T.; Allen, C.D.; Munson-McGee, S.; Havstad, K.M. Cross-Scale Interactions, Nonlinearities, and Forecasting Catastrophic Events. *Proc. Natl. Acad. Sci. USA* **2004**, *101*, 15130–15135. [CrossRef] [PubMed]
65. Chang, X.; Wang, B.; Yan, Y.; Hao, Y.; Zhang, M. Characterizing Effects of Monsoons and Climate Teleconnections on Precipitation in China Using Wavelet Coherence and Global Coherence. *Clim. Dyn.* **2019**, *52*, 5213–5228. [CrossRef]
66. Torrence, C.; Compo, G.P. A Practical Guide to Wavelet Analysis. *Bull. Am. Meteorol. Soc.* **1998**, *79*, 61–78. [CrossRef]
67. Partal, T.; Küçük, M. Long-Term Trend Analysis Using Discrete Wavelet Components of Annual Precipitations Measurements in Marmara Region (Turkey). *Phys. Chem. Earth Parts A/B/C* **2006**, *31*, 1189–1200. [CrossRef]

Disclaimer/Publisher's Note: The statements, opinions and data contained in all publications are solely those of the individual author(s) and contributor(s) and not of MDPI and/or the editor(s). MDPI and/or the editor(s) disclaim responsibility for any injury to people or property resulting from any ideas, methods, instructions or products referred to in the content.